Effect of temperature cycle on mechanical properties of methane hydrate-bearing sediment

Thi Xiu Le, Patrick Aimedieu, Michel Bornert, Baptiste Chabot, Stéphane Rodts, Anh Minh A.M. Tang

HAL Id: hal-02504078
https://enpc.hal.science/hal-02504078

Submitted on 10 Mar 2020

Effect of temperature cycle on mechanical properties of methane hydrate-bearing sediment

Thi Xiu Le, Patrick Aimedieu, Michel Bornert, Baptiste Chabot, Stéphane Rodts, Anh Minh Tang

Laboratoire Navier (UMR8205 IFSTTAR-ENPC-CNRS), Université Paris Est, Marne-la-vallée, France

Corresponding author:

Dr. Anh Minh TANG

Ecole des Ponts ParisTech

6-8 av. Blaise Pascal, Cité Descartes, Champs-sur-Marne

F-77455 Marne – la – Vallée cedex - France

E-mail: anh-minh.tang@enpc.fr

15   ***Abstract***

16   In this study, methane hydrate-bearing sand (MHBS) was created in the laboratory following

17   two methods in order to obtain two types of gas hydrate morphology in sandy sediment. The

18   hydrate morphology in the sediment was assessed by measuring the compressional wave

19   velocity combined with models to predict the wave velocities of the sediment containing gas

20   hydrates. The mechanical properties of the MHBS were investigated by triaxial compression

21   tests. The results obtained by the compressional wave velocity show that after saturating the

22   MHBS sediment (created by the excess gas method) with water, the methane hydrates are partly

23   or completely converted from grain contacts to pore spaces depending on the hydrate saturation

24   (ranging from 0 to 50%). A subsequent temperature cycle completes this conversion process

25   for high hydrate saturation. The results obtained with the triaxial compression tests show higher

26   shear strength, a higher secant Young's modulus, and a higher dilation angle at higher hydrate

27   saturation. In addition, the effects of hydrate saturation on the mechanical properties of the

28   MHBS obtained by the two procedures (with and without the thermal cycle) are similar at low

29   hydrate saturation. The effect of gas hydrate morphologies can only be detected in the case

30   where the conversion (and/or redistribution) of gas hydrates from grain contacts to pore spaces

31   is not complete (at high hydrate saturation).

32

33   ***Key words****: methane hydrate, sand, mechanical behavior, pore habit, rock physics model.*

34

1. Introduction

Methane hydrates, being solid ice-like compounds of methane and water, form naturally at high pressure and low temperature. Due to the growing energy demand, natural gas hydrates (primarily methane hydrates) are being considered as an alternative energy source (Collett et al., 2009). However, methane hydrate dissociation during borehole drilling and the production process (with heat or depressurization methods) may reduce the strength of the hydrate-bearing sediments and cause failure (Nixon and Grozic, 2007). In addition, slope instability and wide-scale gas venting are the two most important geo-hazards associated with methane hydrate dissociation problems on the sea floor (Collett et al., 2014; Sultan et al., 2004). For these purposes, various studies have been performed to investigate the mechanical behavior of methane hydrate-bearing sediments.

In natural sediments, methane hydrates exist in the form of nodules/chunks, lenses/veins or pore-filling depending on the characteristic particle size and effective stress (Dai et al., 2012; Konno et al., 2015; Masui et al., 2008). After Collett et al. (2009), the majority (90%) of methane hydrates is said to be found in fine-grained sediments in dispersed forms, but hydrate saturation is typically low. On the contrary, the larger pore size and relatively high permeability of sandy sediments facilitate methane hydrate formation as pore-filling with high hydrate saturation. For this reason, methane hydrate-bearing sand (MHBS) is the actual target for potential gas hydrate exploration within the scope of future gas production.

In spite of the various numerical models (Jiang et al., 2014; Pinkert & Grozic, 2014; Sánchez et al., 2017; Uchida et al., 2012), few experimental works exist on the investigation of the mechanical behavior of MHBS. Among the existing experimental studies, few works focus on

59   intact samples (Masui et al., 2008; Winters et al., 2007; Yoneda et al., 2015, 2017). Almost all

60   the experimental works are concerned with laboratory tests on synthetic samples because of the

61   challenges involved with getting cored intact methane hydrate-bearing sediment samples. With

62   recent advances in core pressure technology (pressure-core analysis and transfer system -

63   PCATs), the temperature and pressure of samples can be maintained within hydrate stability so

64   that mechanical tests on almost undisturbed samples can be done. However, improvements are

65   still needed to increase the successful pressuring core proportion and to efficiently extrude

66   samples into the PCAT's triaxial cell (Priest et al., 2015; Yamamoto, 2015; Yoneda et al., 2017,

67   2015).

68

69   The hydrate morphology in sediments is usually assessed by comparing the measured seismic

70   velocities and those calculated via models (Dvorkin and Nur, 1998, 1996; Helgerud et al.,

71   1999). In the model proposed by Helgerud et al. (1999), four pore-scale hydrate distributions

72   are considered. This model is based on the fact that seismic velocities depend on the bulk elastic

73   moduli of the system, which are controlled by the grain-scale arrangements of the hydrates and

74   the sediment. For a given hydrate saturation, the hydrates floating in the pore fluid (pore-filling

75   morphology) increase the seismic velocity by increasing the modulus of the pore fluid. This has

76   the smallest impact on the host sediment's elastic properties. On the contrary, hydrates forming

77   only at the grain contacts and acting as cement (contact cement morphology) have the greatest

78   impact on the elastic properties of sediments and increase the seismic velocity by locking

79   individual grains together. The hydrates forming part of the sediment frame (load-bearing

80   morphology) are simply considered as a second mineral in the quartz sand pack, while the

81   hydrates surrounding and cementing the sediment grains (grain-coating morphology) are held

82   together by the effective pressure. Their presence dramatically increases the granular contact

83   stiffness by locking the grains in place.

84

85 The relationship between compressional velocity and hydrate saturation is usually used to

86 assess the hydrate pore habit. In sandy samples, the gas hydrates can be created at the contacts

87 between the sand grains in gas-saturated media by various methods: (i) ice seeding (Priest et

88 al., 2005), (ii) excess gas (partial water saturation) without water saturation (Grozic and

89 Ghiassian, 2010; Hyodo et al., 2013a; Waite et al., 2004; Winters et al., 2007; Zhang et al.,

90 2012), (iii) or excess gas (partial water saturation) followed by water saturation (Hyodo et al.,

91 2013a; Miyazaki et al., 2011b). Dissolving the gas is considered as a good method for

92 reproducing natural methane gas hydrate formation in marine sediments, but this method is

93 time-consuming especially at high hydrate saturation due to the low solubility of methane gas

94 in water (Spangenberg et al., 2005). Priest et al. (2009) proposed the water excess method, but

95 methane hydrates formed heterogeneously inside their sample (Kneafsey et al., 2010). Choi et

96 al. (2014) proposed a non-cementing methane hydrate-forming method by combining the

97 excess gas method with saline water injection at restricted conditions and a temperature cycle.

98 However, in the work of Choi et al. (2014), mechanical tests were not performed to investigate

99 the effect of the hydrate pore habit (hydrate morphology) on the mechanical properties of the

100 sediment.

101

102 Without measuring the acoustic properties, Ebinuma et al. (2005) and Masui et al. (2005)

103 formed methane hydrates by the excess gas and ice-seeding methods, determined the

104 mechanical properties of MHBS (by triaxial compression tests), and suggested that pore-filling

105 hydrates could be created by the ice-seeding method.

106

107 In the present work, gas hydrates were created in sandy samples following two methods. The

108   first one corresponds to the creation of methane hydrates in a partial water saturation sample

109   followed by a water saturation phase prior to the mechanical testing. The second one was similar

110   to the first one, but was completed with a temperature cycle (as suggested by Choi et al., 2014).

111   That would lead to two types of hydrate pore habits. The measurement of the compressional

112   wave velocity and triaxial compression tests were used to assess the grain-scale hydrate

113   distribution in sediments. Tests were performed with various hydrate saturations (0 - 50%) to

114   investigate the effect of this parameter on the mechanical properties of the MHBS. It should be

115   noted that gas hydrate-bearing sandy sediments in nature could have higher hydrate saturation

116   (up to 80%). In addition, other researchers (Yoneda et al., 2017; Yun et al., 2007) mentioned

117   that the mechanical properties of hydrate-bearing sediments would change exponentially with

118   hydrate saturation in the range over 40~50%. However, the hydrate pore habit would be more

119   complex in these cases and would need more extensive work.

2. Experimental method

2.1. Materials

122   The soil used in this study was Fontainebleau silica sand (NE34). Its mechanical properties are

123   generally well-documented (Dupla et al., 2007). It consists of poor-graded sub-rounded grains

124   having diameters ranging from 100 to 300 microns (the particle size distribution curve shown

125   in Figure 1 was obtained by laser diffraction analysis). Tap water was used in the tests. The

126   standard purity of the methane gas used here was 99.995%.

2.2. Experimental setup

128   Figure 2 presents a schematic view of the temperature-controlled high-pressure triaxial

129   apparatus. The sample (1) was covered with a neoprene membrane, 50 mm in diameter and 100

130   mm in height. A displacement sensor (2) was used to monitor the radial strain of the sample,

131   serving to calculate the volumetric strain during consolidation. For the mechanical loading, the

132 confining pressure was applied to the fluid (silicone oil) inside the cell by a volume/pressure

133 controller (3); the deviator stress, applied via the piston (4), was measured by the force

134 transducer (5) installed above the piston. It should be noted that the friction between the cell

135 and the piston (corresponding to approximately 200 kPa of deviator stress) can be measured

136 when the piston is moved down without touching the top baseplate (10). Methane gas was

137 injected via the bottom inlet (6) by a pressure controller, which was connected to a gas

138 flowmeter. The top and bottom pore pressure transducers were connected by a T-valve (7). The

139 pore water pressure was controlled by a volume/pressure controller (8). For the temperature

140 control, the cell was immersed in a temperature-controlled bath connected with a cryostat. A

141 thermocouple (9) was placed close to the sample to measure the temperature inside the cell. For

142 the measurements of the compressional wave velocities, two ultrasonic sensors were installed

143 on the top and bottom baseplates (10) and connected to a wave generator.

144 ## 2.3. Test procedure

145 MHBS samples were prepared by the following procedure:

146 - Step 1: Moist sand (having a known moisture content) was compacted by tamping in

147   layers to obtain a void ratio of 0.63 inside the neoprene membrane prior to the assembly

148   of the experimental setup, as shown in Figure 2.

149 - Step 2: The sample was consolidated at drained conditions (state 1 in Figure 3). The

150   confining pressure was increased to 25 MPa then decreased to 10 MPa. As the maximal

151   value of confining pressure during the subsequent test was 22 MPa, the consolidation

152   step would ensure that the soil remained in the elastic domain during the whole test.

153 - Step 3: To create methane hydrates inside the sample, the temperature of the bath was

154   decreased to 3 – 4°C and vacuum was applied to eliminate the pore air in the sample.

155   Afterward, methane gas was injected at 7 MPa during the whole methane hydrate

156   formation period (state 2 in Figure 3). The methane hydrate formation in gas-saturated

157 media was considered complete when the methane gas flow rate became negligible (<

158 0.1 ml/min). At the end of this step, methane hydrate saturation can be estimated from

159 the initial water saturation (an increase in volume of 10% was considered due to the

160 water-hydrate shift). It should be noted that 7 MPa of gas pressure is much higher than

161 the value required to create gas hydrates at a temperature of 3 - 4°C (see state 2 in Figure

162 3). In addition, preliminary studies have shown that the ultrasonic sensors could

163 correctly measure the compressional wave velocities only in the case of an effective

164 stress higher than 1 MPa (Ebinuma et al., 2008; Rydzy and Batzle, 2010). For this

165 reason, a confining pressure of 10 MPa (corresponding to an effective stress of 3 MPa)

166 was chosen.

167 - Step 4: To saturate the MHBS sample, the T-valve (7) was opened to the atmosphere

168 for a short period (about 10 s) to let the excess gas (initially under a pressure of 7 MPa)

169 escape from the sample (i.e., the pore pressure decreased to zero) and then this valve

170 was connected to the volume/pressure controller (8) to inject water with a pressure of 7

171 MPa. This procedure allowed the excess gas to be replaced in the sample by water and

172 minimized the disturbance of methane hydrates that already existed inside the sample

173 by saturating the sample without circulating water.

174 After the above steps had been completed, two different procedures were used:

175 - For procedure A, a drained triaxial compression test was performed directly after

176 verifying the good saturation of the sample at 22 MPa of confining pressure and 19 MPa

177 of pore pressure by mean of Skempton's coefficient.

178 - For procedure B, a temperature cycle was performed beforehand to modify the gas

179 hydrate distribution at the grain scale. For this purpose, the pore pressure and the

180 confining pressure were first decreased from 7 MPa to 4 MPa and from 10 MPa to 7

181 MPa, respectively. All the drainage valves were then closed and the temperature of the

182   cell was increased to higher than 20°C. That corresponds to a heating of the sample

183   under undrained conditions in order to progressively dissociate the existing gas

184   hydrates. During this phase, the pore pressure (measured by the pressure transducer)

185   increased progressively because of the heating. A Labview program was used to

186   automatically control the confining pressure (via the volume/pressure controller (3)) in

187   order to maintain the mean effective stress (confining pressure minus pore pressure) at

188   3 MPa. When the pore pressure reached 19 MPa and the confining pressure reached 22

189   MPa, the T valve (7) was opened for connection with the volume/pressure controller

190   (8). During this step, the pressure in the volume/pressure controller (8) was maintained

191   at 19 MPa and the volume of water expelled during this heating period was monitored.

192   The gas hydrates were supposed to be totally dissociated when the volume of expelled

193   water had stabilized. After this dissociation phase, gas hydrates were then reformed in

194   the sample by decreasing the temperature of the cell to 3-4°C, while maintaining the

195   pore pressure at 19 MPa (and the confining pressure at 22 MPa). This phase induced an

196   injection of water from the volume/pressure controller (8) to the sample. The hydrate

197   reformation phase was considered to be finished when the volume of injected water had

198   stabilized. After the gas hydrate reformation, a drained triaxial compression test was

199   performed under an effective confining pressure of 3 MPa as in the case of tests using

200   procedure A.

201 In the pore pressure vs temperature plot (Figure 3), procedure A follows the path (1)-(2)-(3),

202 while procedure B follows the path (1)-(2)-(4)-(3). The axial strain rate for all the triaxial

203 compression tests was fixed at 0.1%/min to ensure the drainage conditions. The final methane

204 hydrate saturation was determined by measuring the volume of methane gas dissociated at the

205 end of the triaxial compression tests.

2.4. Test program

The test program is shown in Table 1. Four tests were performed with procedure A (A1 to A4) and four tests were performed with procedure B (B1 to B4). The moisture content was imposed prior to the sample preparation. The water saturation was calculated from the imposed moisture content, the void ratio obtained after the sample preparation ($e = 0.63$), and the particle density ($\rho_s = 2.65$ Mg/m^3). In addition, a reference test was performed, which consisted of compacting dry sand down to a void ratio of 0.63 in the triaxial cell. After the consolidation step (confining pressure was increased to 25 MPa and then decreased to 10 MPa), the sample was saturated with water at a confining pressure of 10 MPa and a water pressure of 7 MPa. Finally, a triaxial compression phase at 22 MPa of confining pressure and 19 MPa of pore pressure was applied as with the other samples. The hydrate saturations shown in Table 1 were determined at the end of the tests from the volume of methane gas dissociated from the sample.

3. Experimental results

3.1. Isotropic consolidation

Figure 4 and Figure 5 show the void ratio (e) and the compressional wave velocity (V_p) versus mean effective stress (p'), respectively, during the consolidation step for all tests (Step 2). The points of the unloading phase correspond to the decrease in confining pressure from 25 MPa to 10 MPa followed by the injection of methane gas at 7 MPa. The compression curves ($e - p'$ plot) show a decrease in void ratio from 0.63 to 0.58-0.59 during the loading path (up to $p' = 25$ MPa). During the unloading path, the void ratio increases to $0.60 - 0.61$ (when $p' = 3$ MPa). The effect of the moisture content on the compression behavior is not clear; the small discrepancy in the results can be then related to the good repeatability of the experimental procedure.

230   Unlike the compression curves ($e - p'$ plot), where hysteresis can be observed during the

231   loading/unloading paths, the relationship between V_p and p' shows reversible behavior (Figure

232   5). Actually, during the loading path when p' increases from 1.6 MPa to 25 MPa (the ultrasonic

233   sensors used in this study could not measure V_p lower than 700 m/s), V_p increases from 750 –

234   850 m/s to 1400 – 1500 m/s. During the unloading path when p' is decreased to 3 MPa, V_p

235   decreases to 900 – 1000 m/s. The results obtained in the consolidation step confirm that V_p is

236   strongly dependent on the mean effective stress (Zimmer, 2004), whereas it is independent of

237   the void ratio and moisture content. For instance, when p' equals 3 MPa, the void ratio at the

238   loading path is higher than that at the unloading path, but the V_p obtained by the two paths are

239   similar. This can be explained by the small volumetric strain (3%). In addition, the results

240   shown in the $V_p - p'$ plot for all the samples (having various moisture contents) are similar.

241   Actually, the matric suction in sand (few kPa, after Feia *et al.*, 2016) is much smaller than the

242   mean effective stress. All the subsequent measurements of V_p were performed at the same mean

243   effective pressure (3 MPa). The discrepancy on the V_p (around ±50 m/s) can be attributed to the

244   repeatability of the experimental procedure.

245   **3.2. Methane hydrate formation**

246   Figure 6 plots V_p versus elapsed time during the methane hydrate formation (Step 3) in gas-

247   saturated media (the confining pressure was maintained at 10 MPa and the gas pressure at 7

248   MPa). At the beginning, V_p equals 900 – 1000 m/s, corresponding to $p' = 3$ MPa. V_p increases

249   slightly during the first minutes and then starts to increase quickly. The first period can be

250   identified as the induction time that is necessary to create the first crystals of methane hydrates

251   (Natarajan et al., 1994). In this study, the induction time is approximately 0.2 h. After the

252   induction time, V_p increases quickly during the next 10 h to progressively reach stabilization.

253   The kinematic of V_p evolution within elapsed time is generally independent of the water

254   saturation. The final value of V_p, however, depends on the initial water saturation and this

255   dependency will be analyzed later. It should be noted that the flow rate of the gas injection at

256   the beginning was much higher than the limit of the flowmeter. For this reason, the total quantity

257   of injected gas could not be measured by the flowmeter.

258

259   Figure 7 shows V_p versus elapsed time during the water saturation (Step 4). It should be noted

260   that time zero corresponds to the beginning of the gas-water shift. For the reference test, V_p

261   increases when the sample is saturated with water. In contrast, for all tests with methane

262   hydrates, replacing the excess methane gas with water decreases V_p.

263

264   As mentioned above, for the tests following procedure A, triaxial compression tests were

265   performed after the water saturation (Step 4) at 22 MPa of confining pressure and 19 MPa of

266   pore pressure, while for the tests following procedure B, a heating/cooling cycle was applied

267   beforehand to dissociate and recreate the methane hydrates inside the sample. The results

268   obtained during the heating path (procedure B) are shown in Figure 8. After decreasing the

269   pore pressure from 7 MPa to 4 MPa, all the inlets were closed. Afterward, the sample was

270   heated in undrained conditions inducing the increase in pore pressure. The pore pressure

271   reached 19 MPa when the temperature of the cell reached 20°C. As mentioned above, when the

272   pore pressure reached 19 MPa, the volume/pressure controller (8) was connected to the sample

273   to maintain the pore pressure at 19 MPa, while the temperature of the cell continued to be

274   increased. Figure 8c plots the volume of water (and/or methane gas) expelled during this phase.

275   It varies from 4×10^{-6} m^3 to 15×10^{-6} m^3, which corresponds to 5% and 20%, respectively, of the

276   pore volume. In addition, the sample having the higher initial water saturation (higher hydrate

277   saturation) shows a higher volume of expelled water.

278

279   Figure 9 presents pore pressure versus cell temperature during this heating path. The phase

280   diagram (relationship between gas pressure and temperature during the dissociation of methane

281   hydrates) is also plotted (Sloan & Koh, 2008). The results show that during this undrained

282   heating path, the $p - T$ plots closely follow the phase diagram (confirming the presence of

283   methane hydrates in the system, after Kwon et al., 2008). However, at a given pressure, the cell

284   temperature (T) is slightly higher than the corresponding temperature determined by the phase

285   diagram. This can be explained by the partial dissociation of hydrates and the continuous

286   heating process (Figure 8a) where the cell temperature is slightly higher than the sample

287   temperature (see also the schematic view of the cell in Figure 2). The $p - T$ plots would be

288   closer to the phase diagram if the heating rate was smaller.

289

290   After this dissociation step, to reform gas hydrates, the pore pressure was maintained at 19 MPa,

291   while the cell temperature was decreased to $3 - 4$°C (except for test B2). Figure 10 shows the

292   cell temperature and the volume of water injected into the sample versus the elapsed time during

293   this step. Except for the case of test B4, the volume of water injected into the sample is similar

294   to that expelled (shown in Figure 8c) and reaches stabilization after 100 h. The volume

295   measured in test B4 continues to increase with a constant rate even after 120 h. This was then

296   attributed to a possible leakage in the connection that occurred due to the heating/cooling cycle.

297   For test B2, the temperature was first decreased to 15°C, hydrate reformation started and

298   became remarkable after 2 hours. The temperature was finally set at 3-4°C like in the other

299   tests.

3.2. Compressional wave velocity

301   Figure 11 shows V_p at different steps during the methane hydrate formation process for all the

302   tests. After the consolidation (Step 2), V_p equals to $900 - 1000$ m/s for all the samples, as shown

303   in Figure 5 (corresponding to $p' = 3$ MPa). After the formation of methane hydrates under the

304   gas-saturated state (Step 3), V_p increases significantly (it equals 2500 – 3500 m/s). In addition,

305   samples having similar water saturation show similar V_p. The subsequent water saturation (Step

306   4) slightly decreases the V_p of the gas-saturated MHBS samples, while it increases the V_p of the

307   reference sample. These values vary in the range of 1800 – 2600 m/s. After the gas hydrate

308   dissociation phase, the V_p of all the four samples for B decreases and approaches the

309   corresponding values obtained by the end of the consolidation (Step 2); they vary between 1000

310   and 1200 m/s. Finally, the re-creation of gas hydrates increases V_p again to the range obtained

311   before the dissociation step (end of Step 4), namely, between 1800 – 2300 m/s.

312

313   The results obtained at the end of the gas hydrate formation in the gas-saturated state (Step 3)

314   are presented in Figure 12 where V_p is plotted versus hydrate saturation. The hydrate saturation

315   was estimated from the initial water saturation and all the water was supposed to be used to

316   create gas hydrates. It should be noted that this figure shows the results for eight tests, but the

317   samples with the same moisture content have the same V_p (as shown in Figure 11). That reveals

318   a good repeatability of the experimental procedure. These results show a clear effect of gas

319   hydrate saturation on V_p. V_p is higher at a higher hydrate saturation; it increases from 900 –

320   1000 m/s at the reference state (without hydrates) to 3500 m/s at $S_h = 55\%$.

321

322   In order to assess the gas hydrate distribution at the grain scale, the models proposed by

323   Helgerud (2001) were used. To predict the gas-saturated MHBS morphology, Helgerud (2001)

324   proposed two contact models using two different schemes: (*i*) gas hydrates are located only at

325   the grain contacts (contact cement) and (*ii*) gas hydrates evenly envelop the grains (grain

326   coating). The parameters used are shown in TTable 2. The results (Figure 12) show that the

327   experimental data obtained in the present work correspond to the zone delimited by these two

328   models. In addition, at low hydrate saturation ($S_h = 27\%$) the experimental data fit the "grain

329   coating" model, while at high hydrate saturation (S_h = 55%), the "contact cement" model is

330   more appropriate. The intermediate values of S_h correspond to the intermediate values of V_p.

331

332   The results corresponding to the water-saturated state are plotted in Figure 13. In this figure,

333   the hydrate saturation was calculated from the quantity of methane gas dissociated at the end

334   of each test (the gas that dissolved in water was ignored). The data obtained after the gas hydrate

335   reformation, with the temperature cycle (only for procedure B), are plotted with closed symbols,

336   while the data obtained without the temperature cycle (for procedure A tests) and before the

337   temperature cycle (for procedure B tests) are plotted with open symbols. It should be noted that,

338   for procedure B, V_p decreases after the temperature cycle in tests B2, B3 and B4, while it

339   remains constant in test B1. Unlike the case of the gas-saturated state, the effect of hydrate

340   saturation is less significant. V_p increases from 1850 m/s for the reference case (without

341   hydrates) to 2500 m/s for S_h = 50%. In addition, the V_p obtained after water saturation (Step 4)

342   is generally higher than that obtained after the dissociation/recreation cycle at a given hydrate

343   saturation.

344

345   In order to assess the gas hydrate distribution of water-saturated MHBS at the grain scale, four

346   models proposed by Helgerud (2001) were used. In addition to the two contact models

347   presented above, a model considering hydrates as fluid components (pore-filling) and another

348   considering hydrates as sediment frame components (load-bearing) were used. The

349   experimental and the models' results are plotted in Figure 13 and show that after water

350   saturation, the V_p data match the "load-bearing" model for some cases and are higher than the

351   predicted value for other cases. After the temperature cycle (procedure B), the experimental

352   data correspond to the pore-filling model, except for test B4 (S_h = 42%), where it is close to the

353   load-bearing model.

3.3. Triaxial compressive properties

354

355 The results obtained from the drained triaxial compression tests are shown in Figure 14 where

356 deviator stress (q) and volumetric strain (ε_v) are plotted versus axial strain (ε_a). It should be

357 noted that all these samples were consolidated at 25 MPa of effective pressure prior to being

358 unloaded to 3 MPa. The creation of methane hydrates and triaxial compression were performed

359 at a mean effective stress of 3 MPa. The confining pressure and pore pressure were maintained

360 at 22 MPa and 19 MPa, respectively, via the volume/pressure controller, while the axial strain

361 rate was fixed at 0.1%/min. The volumetric strain was calculated based on the volume of water

362 entering/being expelled from the sample. The results obtained from all the tests are quite

363 similar: (*i*) the deviator increases almost linearly at the beginning, it reaches a peak value at

364 about 2-3% of axial strain and decreases progressively to reach a residual state; (*ii*) the

365 volumetric strain shows small contraction at the beginning and then decreases significantly

366 (dilatation) prior to reaching the residual state at high axial strain (ε_a larger than 10%) where ε_v

367 remains constant. There is almost no difference between the results of the two procedures.

368

369 The triaxial compressive properties, determined from the results shown in Figure 14, are plotted

370 in Figure 15 versus hydrate saturation (S_h). The peak strength, q_{max}, corresponds to the maximal

371 value of the deviator (Figure 15a); the residual strength, q_{res}, corresponds to the deviator at the

372 end of the test (Figure 15b). The secant Young's modulus, E_{50}, corresponds to the secant

373 stiffness at 50% of the stress difference (Figure 15c). The dilation angle, ψ, is determined from

374 the change in volumetric strain with respect to the change in shear strain by supposing that it is

375 constant between 2 and 4% of the axial strain (Figure 15d). It is obvious that all these values

376 are higher at a higher methane hydrate saturation.

377

378   Figure 16 shows an examination of all test results using Rowe's stress-dilatancy analysis for

379   axial deformations before the peak strength was reached. For triaxial compression test

380   conditions, the model is given by

381
$$\frac{\sigma'_1}{\sigma'_3} = tan^2\left(\frac{\pi}{4} + \frac{\varphi_{cs}}{2}\right)\left(1 - \frac{\dot{\varepsilon}_v}{\dot{\varepsilon}_1}\right)$$

382   where σ'_1 and σ'_3 are the major and minor effective stresses, respectively, $\dot{\varepsilon}_v$ and $\dot{\varepsilon}_1$ are the

383   volumetric and major principal strain rates, respectively, and φ_{cs} is the critical state friction

384   angle (Pinkert, 2017a).

385   All the experimental data are close to the values predicted by the model with $\varphi_{cs} = 25°$, except

386   for tests A3 and A4.

4. Discussion

388   The induction time observed, approximately 0.2 h, is almost independent of the initial moisture

389   content. This is in agreement with the results of Chong et al. (2016) who found an induction

390   time of 0.1-0.8 h for fine sand (0.1 – 0.5 mm) prepared at 75% water saturation. Bagherzadeh

391   et al. (2011) used the magnetic resonance imaging technique to investigate the formation of

392   methane hydrates in an unconsolidated bed of silica sand and found that hydrate formation is

393   not uniform and that the nucleation of hydrate crystals occurs at different times and different

394   positions inside the bed. In addition, the hydrate formation was found to be faster with a lower

395   moisture content and a smaller particle size. In the present work, only one particle size

396   distribution was considered and the water saturation varied in a small range (from 25 to 50%).

397   That would explain the independency of the induction time on the moisture content.

398

399   Figure 12 shows that gas hydrates significantly increase the compressional wave velocity at the

400   gas-saturated state. The observation of the water distribution in the unsaturated sand at the pore

401 scale of Crist et al. (2004) reveals that water can be distributed around the grains as a thin layer

402 (by adsorption) and also at the menisci of the grain contacts (by capillarity). In addition, at low

403 water saturation, the water is mainly distributed at the surface of the grains (because the

404 adsorption suction is much higher than the capillary suction); the volume of water at the menisci

405 becomes dominant only at high water saturation. This was also observed by Riedel et al. (2012)

406 via X-Ray Tomography at various water saturations. The injection of gas hydrates at 7 MPa of

407 pressure and $3 - 4°C$ of temperature induces the transformation of water into the gas hydrates.

408 The results show that this hydrate formation in gas-saturated media increases the V_p (see Figure

409 6), and this increase reaches the stabilization state after about 100 h. This stabilization suggests

410 that almost the entire quantity of available water has been transformed into gas hydrates. In

411 addition, the distribution of gas hydrates should be similar to that of water prior to its creation.

412 As a consequence, at a low moisture content (hydrate saturation), the gas hydrates are mainly

413 distributed around the grains, while at a high moisture content (hydrate saturation), the role of

414 the gas hydrates at the grain contacts dominates. This explanation is in agreement with the

415 comparison between the experimental data and Helgerud's model shown in Figure 12.

416 Chaouachi et al. (2015) investigated the formation of Xenon gas hydrates in under-saturated

417 sediments with juvenile water using synchrotron X-ray computed tomographic microscopy.

418 The results showed that the nucleation started at the water-gas interface resulting in an initial

419 gas hydrate film, several micrometers in thickness, and future growth proceeded to form

420 isometric single crystals, $10 - 20$ micron in size. In the study of Yoneda et al. (2016), the

421 formation of krypton hydrates in partially saturated sand was observed using micro-focus X-

422 ray computed tomography. The results also confirmed the formation of hydrates from the

423 capillary bridges of wet sand and the patchy initial distribution of water.

424

425   After the formation of gas hydrates in gas-saturated state, the subsequent water saturation phase

426   significantly decreases the V_p (Figure 7). Ebinuma et al. (2008) and Kneafsey et al. (2010)

427   observed a similar decrease in sonic velocities when saturating the gas-saturated MHBS with

428   water. Hyodo et al. (2013) compared the mechanical properties of gas-saturated MHBS with

429   those of water-saturated ones (using the same sand under the same stress conditions) and found

430   higher stiffness and higher failure strength for gas-saturated specimens. It should be noted that

431   the procedure applied by Hyodo et al. (2013) to obtain water-saturated MHBS is similar to

432   procedure A used in the present work. These results suggest that water saturation modifies the

433   hydrate distribution at the grain scale; the gas hydrates located at the grain contacts would be

434   progressively converted or/and redistributed into the pore spaces (Choi et al., 2014). In this

435   study, the effect of water injection in gas-saturated hydrate-bearing sediments is investigated at

436   different levels of hydrate saturation. The results shown in Figure 7 and Figure 13 indicate that

437   this process takes longer for higher hydrate saturation. For some specimens (B2, B4, A3, and

438   A4), this transformation was not complete when the subsequent step (triaxial compression for

439   specimens A and heating/cooling cycle for specimens B) was applied. This can be explained

440   by the higher values for V_p than the predicted values of the load-bearing model. In addition, for

441   the two tests following procedure A (A3 and A4), even after waiting a long time for water

442   saturation (to make sure that the MHBS was well saturated with water), the V_p were still higher

443   than the values predicted with the load-bearing model. This can perhaps be explained by the

444   patchy hydrate distribution suggested by Dai et al. (2012) where the bulk stiffness approaches

445   the lower Voigt-Reuss bound at low hydrate saturation and the upper bound at high hydrate

446   saturation due to the mechanical interaction between the hydrate-saturated patches. As

447   aforementioned, the number of tests is not so high, but the procedure was correctly controlled

448   in the laboratory. The repeatability of the tests can be appreciated from the results of the

449   consolidation step (Step 2), seen in Figure 4 and Figure 5, and the hydrate formation in gas-

450   saturated media (Step 3), seen in Figure 6.

451

452   In the present work, methane gas was injected into an unsaturated sand specimen to create a

453   MHBS sample. Afterward, water was injected to saturate the specimen. This procedure is

454   similar to that used by Miyazaki et al. (2011) and Hyodo et al. (2013) to investigate the triaxial

455   compressive properties of artificial MHBS. As the initial distribution of water inside the

456   specimen should be homogenous (partly due the equilibrium of the capillary force), it was

457   expected that the distribution of gas hydrates inside the sample would also be homogenous

458   within this method. However, Kneafsey et al. (2010), using X-ray computed tomography,

459   found that this method produced both well-distributed hydrates and very heterogeneous

460   hydrates. They noted that the heterogeneity in the hydrate saturation (observed in the work of

461   Seol & Kneafsey, 2009) was affected by the initial sample heterogeneity, but not dominated by

462   it. In the present work, as the sand specimen was well compacted, the specimen density was

463   relatively homogenous. As a result, the gas hydrate distribution is expected to be homogenous.

464   Observation by magnetic resonance imaging (MRI) on a sample prepared by the same

465   procedure has confirmed this statement (see Le et al., 2019).

466

467   The subsequent heating/cooling cycle aims at dissociating/recreating gas hydrates without

468   disturbing the homogeneity of the hydrate distribution. For this reason, during the heating path,

469   the drainage system was closed during the first period. This condition induced an increase in

470   pore pressure (Figure 8 and Figure 9) mainly due to thermal dilation of water and hydrate

471   dissociation (Kwon et al., 2008). The undrained heating condition was stopped when the pore

472   pressure approached the limit of the pore pressure transducer (20 MPa). A small quantity of

473   water (and dissolved methane gas) was then allowed to be expelled. As the final state (in terms

474   of pore pressure and temperature) is far outside the phase diagram (Figure 9), the methane

475   hydrates should be completely dissociated at the end of the heating path. During the subsequent

476   cooling path, the pore pressure was maintained at 19 MPa, and the cooling induced the injection

477   of water to the specimen (Figure 10). This corresponds mainly to both the thermal contraction

478   of water and the gas hydrate reformation. The reformation of gas hydrates can be easily

479   identified when the cell temperature remains constant, while the volume of injected water

480   increases abruptly (e.g., at 12 h for test B2).

481

482   Choi et al. (2014) formed methane hydrates with the partial water saturation method (excess

483   gas method), injecting saline water at locations just outside of the hydrate stability zone for

484   saline water and doing a temperature cycle. It was concluded that slow saline water injection is

485   the key to initiating the formation of non-cementing hydrates and that the temperature cycle

486   ensured this formation. The V_P after warming was quite high, while the sample was not

487   saturated. The hydrate dissociation was perhaps not completed before the hydrate reformation.

488   This explains why the difference in V_p between after the saline water injection and after the

489   temperature cycle was not obvious. The measurement of V_p at the end of the thermal cycle in

490   the present study is smaller than that obtained after water saturation. In addition, it fits with the

491   pore-filling and load-bearing models. It can then be expected that the heating/cooling cycle

492   allows for the completion of the conversion of the hydrate accumulation habit into the non-

493   cementing type.

494

495   The experimental results obtained from the triaxial compression tests show higher values for

496   the maximum deviator stress, secant Young's modulus, residual deviator stress, and dilation

497   angle at a higher hydrate saturation. Hyodo et al. (2013) and Miyazaki et al. (2011) found a

498   similar effect for the hydrate saturation on the maximum deviator stress and secant Young's

499 modulus while testing the MHBS prepared with a procedure similar to procedure A in the

500 present work. The effect of the methane hydrate saturation on the stiffness and failure strength

501 of MHBS was explained by particle bonding. However, the measurement of V_p in the present

502 work suggests that grain-contact hydrates have been significantly converted into non-grain-

503 contact (non-cementing) types by the end of procedure A, as explained above. In addition, the

504 results obtained by procedure B (where the conversion has already been completed) show a

505 similar effect of the hydrate saturation on the stiffness and failure strength of MHBS. Soga et

506 al. (2006) showed a similar increase in the dilation angle with an increase in the hydrate

507 saturation for natural samples and synthetic samples (partial water saturation method for strong

508 grain contacts and ice-seeding method for weak grain contacts) at 1 MPa of confining pressure.

509 It is obvious that an increase in the hydrate saturation enhances the dilative characteristics of

510 soils, and this increase is more apparent when the hydrate saturation exceeds 30%. Recently,

511 Pinkert (2017a,b) analyzed the experimental data obtained by a procedure similar to procedure

512 A and also concluded that no cohesive effect was found when interpreting the test results under

513 a stress-dilatancy framework.

514

515 In the present work, the cohesion and friction angle cannot be determined because only one

516 level of effective confining pressure was used. For this reason, the approach of Pinkert

517 (2017a,b) can be appropriated to give more information about the cohesion. When using the

518 method proposed by Pinkert (2017a) to analyze the data obtained in the present work (Figure

519 16), the results from tests A3 and A4 are positioned above the other curves. These results then

520 correspond to a significant increase in the degree of cohesion in the samples. This is also in

521 agreement with the results shown in Figure 13 and the above comments in which it is expected

522 that the conversion of gas hydrates from grain contacts to pore spaces is not completed for these

523 two cases. To simulate natural hydrate-bearing sediments, with a range in hydrate saturation of

524   0-50%, procedure A (without the temperature cycle) could be used when the hydrate saturation

525   is smaller than 40%, while at higher saturation (40-50%), a temperature cycle should be added

526   (procedure B should be used).

Conclusions

528   Methane hydrate-bearing sand was first created by pressurizing methane gas (at 7 MPa) into an

529   already chilled moistened packed sandy specimen (excess gas method). Following the hydrate

530   formation, water was injected into the sample and the remaining gas was simultaneously bled

531   out. The water pressure was then maintained at 19 MPa (22 MPa of confining pressure) until

532   water was no longer injected into the sample. That corresponds to the end of procedure A for

533   preparing the MHBS specimen. For procedure B, a subsequent heating/cooling cycle was

534   applied in order to completely dissociate the gas hydrates and then recreate them inside the

535   specimen. Measurement of the compressional wave velocity was performed along with these

536   processes, while triaxial compression tests were performed at the end of each procedure. Rock

537   physics models were also compared to the experimental data to assess the grain scale

538   distribution of the gas hydrates at each state. The following conclusions can be drawn:

539   - Pressurizing methane gas into an already chilled moistened packed sandy specimen

540   creates gas hydrates at the grain contacts. This excess gas method allows for a

541   significant increase in V_p.

542   - Subsequent water saturation converts (and/or redistributes) the gas hydrates from grain

543   contacts to pore spaces and, as a result, decreases V_p. This process may take several

544   days, depending on the hydrate saturation, and cannot be completed for high hydrate

545   saturation.

546   - The heating/cooling cycle allows for the completion of the conversion (and/or

547   redistribution) of gas hydrates from grain contacts to pore spaces.

548 - The effects of hydrate saturation on the mechanical properties of MHBS obtained by
549 the two procedures (with and without thermal cycles) are similar at low hydrate
550 saturation.

551 - The effect of the grain scale gas hydrate distribution can be detected in the case where
552 the conversion (and/or redistribution) of gas hydrates from grain contacts to pore spaces
553 is not complete.

554 As the non-cementing habit is actually the most representative case of natural gas hydrate-
555 bearing sandy sediments, the findings of the present work would be helpful for future studies
556 on gas hydrate-bearing sediments in the laboratory. Actually, within procedure A, non-
557 cementing hydrates could be obtained by waiting long enough for the completion of the hydrate
558 conversion from grain contacts to pore spaces in the case of small hydrate saturation. With the
559 heating/cooling cycle (procedure B), non-cementing hydrates could even be obtained at higher
560 hydrate saturation.

Acknowledgements

References

568 Bagherzadeh, S.A., Moudrakovski, I.L., Ripmeester, J.A., Englezos, P., 2011. Magnetic
569 Resonance Imaging of Gas Hydrate Formation in a Bed of Silica Sand Particles. Energy
570 Fuels 2011 25, 3083–3092. doi:10.1021/ef200399a

571   Chaouachi, M., Falenty, A., Sell, K., Enzmann, F., Kersten, M., Haberth, D., Werner, F.K.,

572   2014. Microstructural evolution of gas hydrates in sedimentary matrices observed with

573   synchrotron X-ray computed tomographicmicroscopy. Geochemistry, Geophys.

574   Geosystems 1009–1020. doi:10.1002/2013GC005162

575   Choi, J.-H., Dai, S., Cha, J.-H., Seol, Y., 2014. Laboratory formation of noncementing hydrates

576   in sandy sediments. Geochemistry, Geophys. Geosystems 15, 1648–1656.

577   doi:10.1002/2014GC005287

578   Chong, Z.R., Yang, M., Khoo, B.C., Linga, P., 2016. Size Effect of Porous Media on Methane

579   Hydrate Formation and Dissociation in an Excess Gas Environment. I&EC Res. 55,

580   7981−7991. doi:10.1021/acs.iecr.5b03908

581   Collett, T., Bahk, J., Baker, R., Boswell, R., Divins, D., Frye, M., Goldberg, D., Husebø, J.,

582   Koh, C., Malone, M., Morell, M., Myers, G., Shipp, C., Torres, M., 2014. Methane

583   Hydrates in Nature - Current Knowledge and Challenges. J. Chem. Eng. data 60, 319–329.

584   Collett, T.S., Johnson, A.H., Knapp, C.C., Boswell, R., 2009. Natural gas hydrates: A review.

585   Am. Assoc. Pet. Geol. 89, 146–219. doi:10.1306/13201101M891602

586   Crist, J.T., McCarthy, J.F., Zevi, Y., Baveye, P.C., Throop, J. A., Steenhuis, T.S., 2004. Pore-

587   Scale Visualization of Colloid Transport and Retention in Partly Saturated Porous Media.

588   Vadose Zo. J. 3, 444–450. doi:10.2113/3.2.444

589   Dai, S., Santamarina, J.C., Waite, W.F., Kneafsey, T.J., 2012. Hydrate morphology: Physical

590   properties of sands with patchy hydrate saturation. J. Geophys. Res. B Solid Earth 117.

591   doi:10.1029/2012JB009667

592   Dupla, J.C., Pedro, L.S., Canou, J., Dormieux, L., 2007. Comportement mécanique de sols

593   grossiers de référence. Bull. des Lab. des Ponts Chaussees 31–57. doi:10.3233/978-1-

594   60750-031-5-64

595   Dvorkin, J., Nur, A., 1998. Acoustic signatures of patchy saturation. Int. J. Solids Struct. 35,

596   4803–4810. doi:10.1016/S0020-7683(98)00095-X

597   Dvorkin, J., Nur, A., 1996. Elasticity of high-porosity sandstones: Theory for two North Sea

598   data sets. Geophysics 61, 890–893. doi:10.1190/1.1444059

599   Ebinuma, T., Suzuki, K., Nagao, J., Oyama, H., Narita, H., Hydrate, M., 2008. OTC 19260

600   Ultrasonic Wave Velocities Associated with Formation and Dissociation of Methane

601   Hydrate in Artificial Sandy Sediment, in: Offshore Technology Conference (OTC).

602   Houston, Texas. doi:10.4043/19260-MS

603   Ebinuma, T., Kamata, Y., Minagawa, H., Ohmura, R., Nagao, J., Narita, H., 2005. Mechanical

604   Properties of Sandy Sediment Containing Methane Hydrate, in: The 5th International

605   Conference on Gas Hydrates. Trondheim, pp. 958–961.

606   Feia, S., Dupla, J.C., Ghabezloo, S., Sulem, J., Canou, J., Onaisi, A., Lescanne, H., Aubry, E.,

607   2015. Experimental investigation of particle suspension injection and permeability

608   impairment in porous media. Geomech. Energy Environ. 3, 24–39.

609   doi:10.1016/j.gete.2015.07.001

610   Grozic, J., Ghiassian, H., 2010. Undrained shear strength of methane hydrate-bearing sand;

611   preliminary laboratory results. Proceeding 6th Can. Permafr. Conf. 63rd Can. Geotech.

612   Conf. 459–466.

613   Helgerud, M.B., 2001. Wave speeds in gas hydrate and sediments containing gas hydrate: a

614   laboratory and modelling study. Dep. Geophys. Stanford University.

615   Helgerud, M.B., Dvorkin, J., Nur, A., 1999. Elastic-wave velocity in marine sediments with gas

616   hy-drates: Effective medium modeling. Geophys. Res. Lett.

617   Hyodo, M., Li, Y., Yoneda, J., Nakata, Y., Yoshimoto, N., Nishimura, A., Song, Y., 2013a.

618   Mechanical behavior of gas-saturated methane hydrate-bearing sediments. J. Geophys.

619   Res. Solid Earth 118, 5185–5194. doi:10.1002/2013JB010233

620   Hyodo, M., Yoneda, J., Yoshimoto, N., Nakata, Y., 2013b. Mechanical and dissociation

621   properties of methane hydrate-bearing sand in deep seabed. Soils Found. 53, 299–314.

622   doi:10.1016/j.sandf.2013.02.010

623   Jiang, M., Chen, H., Tapias, M., Arroyo, M., Fang, R., 2014. Study of mechanical behavior and

624   strain localization of methane hydrate bearing sediments with different saturations by a

625   new DEM model. Comput. Geotech. 57, 122–138. doi:10.1016/j.compgeo.2014.01.012

626   Kneafsey, T.J., Rees, E.V.L., Nakagawa, S., Kwon, T., 2010. Examination of Hydrate

627   Formation Methods : Trying to Create Representative Samples.

628   Konno, Y., Yoneda, J., Egawa, K., Ito, T., Jin, Y., Kida, M., Suzuki, K., Fujii, T., Nagao, J.,

629   2015. Permeability of sediment cores from methane hydrate deposit in the Eastern Nankai

630   Trough. Mar. Pet. Geol. 66, 487–495. doi:10.1016/j.marpetgeo.2015.02.020

631   Kwon, T.H., Cho, G.C., Santamarina, J.C., 2008. Gas hydrate dissociation in sediments:

632   Pressure-temperature evolution. Geochemistry, Geophys. Geosystems 9, 1–14.

633   doi:10.1029/2007GC001920

634   Le, T.X., Rodts, S., Hautemayou, D., Aimdieu, P., Bornert, M., Chabot, B., Tang, A.M., 2019.

635   Kinetics of methane hydrate formation and dissociation in sand sediment. Geomechanics

636   for Energy and the Environment. doi: 10.1016/j.gete.2018.09.007

637   Masui, A., Haneda, H., Ogata, Y., Aoki, K., 2005. The effect of saturation degree of methane

638   hydrate on the shear strength of synthetic methane hydrate sediments, in: The 5th

639   International Conference on Gas Hydrates, Trondheim, Norway. Trondheim, pp. 657–663.

640   Masui, A., Kuniyuki, M., Hironori, H., Yuji, O., Kazuo, A., 2008. Mechanical Properties of

641   Natural Gas Hydrate Bearing Sediments Retrieved from Eastern Nankai Trough, in:

642   Offshore Technology Conference (OTC). Houston, Texas. doi:10.4043/19277-MS

643   Miyazaki, K., Masui, A., Sakamoto, Y., Aoki, K., Tenma, N., Yamaguchi, T., 2011a. Triaxial

644   compressive properties of artificial methane-hydrate-bearing sediment. J. Geophys. Res.

645   Solid Earth 116. doi:10.1029/2010JB008049

646   Miyazaki, K., Tenma, N., Aoki, K., Sakamoto, Y., Yamaguchi, T., 2011b. Effects of confining

647   pressure on mechanical properties of artificial methane-hydrate-bearing sediment in

648   triaxial compression test. Int. J. Offshore Polar Eng. 21, 148–154.

649   Natarajan, V., Bishnoi, P.R., Kalogerakis, N., 1994. Induction phenomena in gas hydrate

650   nucleation. Chem. Eng. Sci. 2509.

651   Nixon, M.F., Grozic, J.L.H., 2007. Submarine slope failure due to gas hydrate dissociation : a

652   preliminary quantification. Can. Geotech. J. 44, 314–325. doi:10.1139/T06-121

653   Pinkert, S., 2017a. Rowe's Stress-Dilatancy Theory for Hydrate-Bearing Sand. Int. J. Geomech.

654   17, 6016008. doi:10.1061/(ASCE)GM.1943-5622.0000682.

655   Pinkert, S., 2017b. The lack of true cohesion in hydrate-bearing sands. Granul. Matter 19, 57.

656   doi:10.1007/s10035-017-0742-5

657   Pinkert, S., Grozic, J.L.H., 2014. Prediction of the mechanical response of hydrate-bearing

658   sands. J. Geophys. Res. Solid Earth 119, 4695–4707. doi:10.1002/2013JB010920

659   Priest, J.A., Best, A.I., Clayton, C.R.I., 2005. A laboratory investigation into the seismic

660   velocities of methane gas hydrate-bearing sand. J. Geophys. Res. B Solid Earth 110, 1–13.

661   doi:10.1029/2004JB003259

662   Priest, J.A., Druce, M., Roberts, J., Schultheiss, P., Nakatsuka, Y., Suzuki, K., 2015. PCATS

663   Triaxial: A new geotechnical apparatus for characterizing pressure cores from the Nankai

664   Trough, Japan. Mar. Pet. Geol. 66, 460–470. doi:10.1016/j.marpetgeo.2014.12.005

665   Priest, J.A., Rees, E.V.L., Clayton, C.R.I., 2009. Influence of gas hydrate morphology on the

666   seismic velocities of sands. J. Geophys. Res. Solid Earth 114. doi:10.1029/2009JB006284

667   Riedel, I., Andò, E., Salager, S., Bésuelle, P., Viggiani, G., 2012. Water Retention Behaviour

668   Explored by X-Ray CT Analysis, in: Unsaturated Soils: Research and Applications. pp.

669   81–88. doi:10.1007/978-3-642-31116-1_11

670   Rydzy, M.B., Batzle, M.L., 2010. Ultrasonic Velocities in Laboratory-Formed Gas Hydrate-

671   Bearing Sediments, in: Symposium on the Application of Geophysics to Engineering and

672   Environmental Problems 2010. Colorado, pp. 615–624. doi:10.4133/1.3445488

673   Sánchez, M., Gai, X., Santamarina, J.C., 2017. A constitutive mechanical model for gas hydrate

674   bearing sediments incorporating inelastic mechanisms. Comput. Geotech. 84, 28–46.

675   doi:10.1016/j.compgeo.2016.11.012

676   Seol, Y., Kneafsey, T.J., 2009. X-ray computed-tomography observations of water flow

677   through anisotropic methane hydrate-bearing sand. J. Pet. Sci. Eng. 66, 121–132.

678   doi:10.1016/j.petrol.2009.01.008

679   Sloan, E.D.J., 2008. Clathrate Hydrates of Natural Gases.

680   Sloan E.D. and Koh C.A., 2007. Clathrate Hydrates of Natural Gases. CRC Press. 752 pages.

681   Soga, K., Ng, M., Lee, S., Klar, A., 2006. Characterisation and engineering properties of

682   methane hydrate soils, in: The 2nd International Workshop on Characterisation and

683   Engineering   Properties   of   Natural   Soils.   pp.   2591–2642.

684   doi:10.1201/NOE0415426916.ch26

685   Spangenberg, E., Kulenkampff, J., Naumann, R., Erzinger, J., 2005. Pore space hydrate

686   formation in a glass bead sample from methane dissolved in water. Geophys. Res. Lett.

687   doi:10.1029/2005GL024107

688   Sultan, N., Cochonat, P., Foucher, J.P., Mienert, J., 2004. Effect of gas hydrates dissociation on

689   seafloor slope stability. Mar. Geol. 213, 379–401. doi:10.1111/j.1551-6709.2009.01091.x

690   Uchida, S., Soga, K., Yamamoto, K., 2012. Critical state soil constitutive model for methane

691 Uchida, S., Soga, K. and Yamamoto, K. Critical state soil constitutive model for methane
692   hydrate soil. J. Geophys. Res., 117, B03209, doi: 10.1029/2011JB008661

693 hyW., Winters, W.J., Mason, D.H., 2004. Methane hydrate formation in partially water-
694   saturated Ottawa sand. Am. Mineral. 89, 1202–1207.

695 Winters, W.J., Waite, W.F., Mason, D.H., Gilbert, L.Y., Pecher, I.A., 2007. Methane gas
696   hydrate effect on sediment acoustic and strength properties. J. Pet. Sci. Eng. 56, 127–135.
697   doi:10.1016/j.petrol.2006.02.003

698 Yamamoto, K., 2015. Overview and introduction: Pressure core-sampling and analyses in the
699   2012-2013 MH21 offshore test of gas production from methane hydrates in the eastern
700   Nankai Trough. Mar. Pet. Geol. 66, 296–309. doi:10.1016/j.marpetgeo.2015.02.024

701 Yoneda, J., Jin, Y., Katagiri, J., Tenma, N., 2016. Strengthening mechanism of cemented
702   hydrate-bearing sand at microscales. Geophys. Res. Lett. 43, 7442–7450.
703   doi:10.1002/2016GL069951

704 Yoneda, J., Masui, A., Konno, Y., Jin, Y., Egawa, K., Kida, M., Ito, T., Nagao, J., Tenma, N.,
705   2015. Mechanical properties of hydrate-bearing turbidite reservoir in the first gas
706   production test site of the Eastern Nankai Trough. Mar. Pet. Geol. 66, 471–486.
707   doi:10.1016/j.marpetgeo.2015.02.029

708 Yoneda, J., Masui, A., Konno, Y., Jin, Y., Kida, M., Katagiri, J., Nagao, J., Tenma, N., 2017.
709   Pressure-core-based reservoir characterization for geomechanics: Insights from gas
710   hydrate drilling during 2012–2013 at the eastern Nankai Trough. Mar. Pet. Geol. 86, 1–
711   16. doi:10.1016/j.marpetgeo.2017.05.024

712 Yun, T.S., Santamarina, C.J., Ruppel, C., 2007. Mechanical properties of sand, silt, and clay
713   containing tetrahydrofuran hydrate. J. Geophys. Res. Solid Earth 112, 1–13.
714   doi:10.1029/2006JB004484

715   Zhang, X.-H., Lu, X.-B., Zhang, L.-M., Wang, S.-Y., Li, Q.-P., 2012. Experimental study on

716   mechanical properties of methane-hydrate-bearing sediments. Acta Mech. Sin. 28, 1356–

717   1366. doi:10.1007/s10409-012-0142-3

718   Zimmer, M.A., 2004. Seismic velocities in unconsolidated sands: Measurements of pressure,

719   sorting, and compaction effects. Stanford University.

720

721

722

Table 1. Test program

Test	Moisture content (%)	Water saturation (%)	Hydrate saturation (%)
Reference	0.0	0	0
A1	6.0	25	21
B1	6.0	25	13
A2	8.5	35	31
B2	8.5	35	34
A3	10.0	42	50
B3	10.0	42	41
A4	12.0	50	48
B4	12.0	50	42

723

Table 2. Parameters used for Helgerud's model

Parameter	Value
Bulk modulus of quartz (GPa)	36.6
Shear modulus of quartz (GPa)	45
Bulk modulus of water (GPa)	2.15
Bulk modulus of air (GPa)	0.01
Porosity (-)	0.387
Density of solid grain (Mg/m^3)	2.65
Density of water (Mg/m^3)	1
Density of air (Mg/m^3)	0
Density of methane hydrate (Mg/m^3)	0.9
Bulk modulus of hydrate (GPa)	7.9
Shear modulus of hydrate (GPa)	3.3
Critical porosity (-)	0.387
Number of contacts per grain (-)	4.5

724
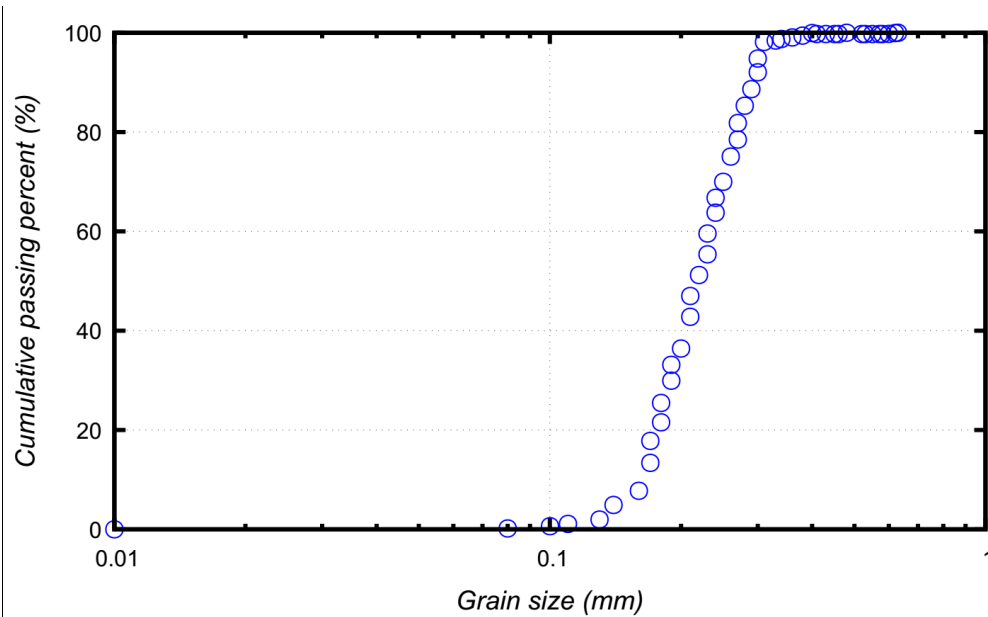
725

726   **Figure 1. Particle size distribution curve (modified from Feia et al., 2015)**
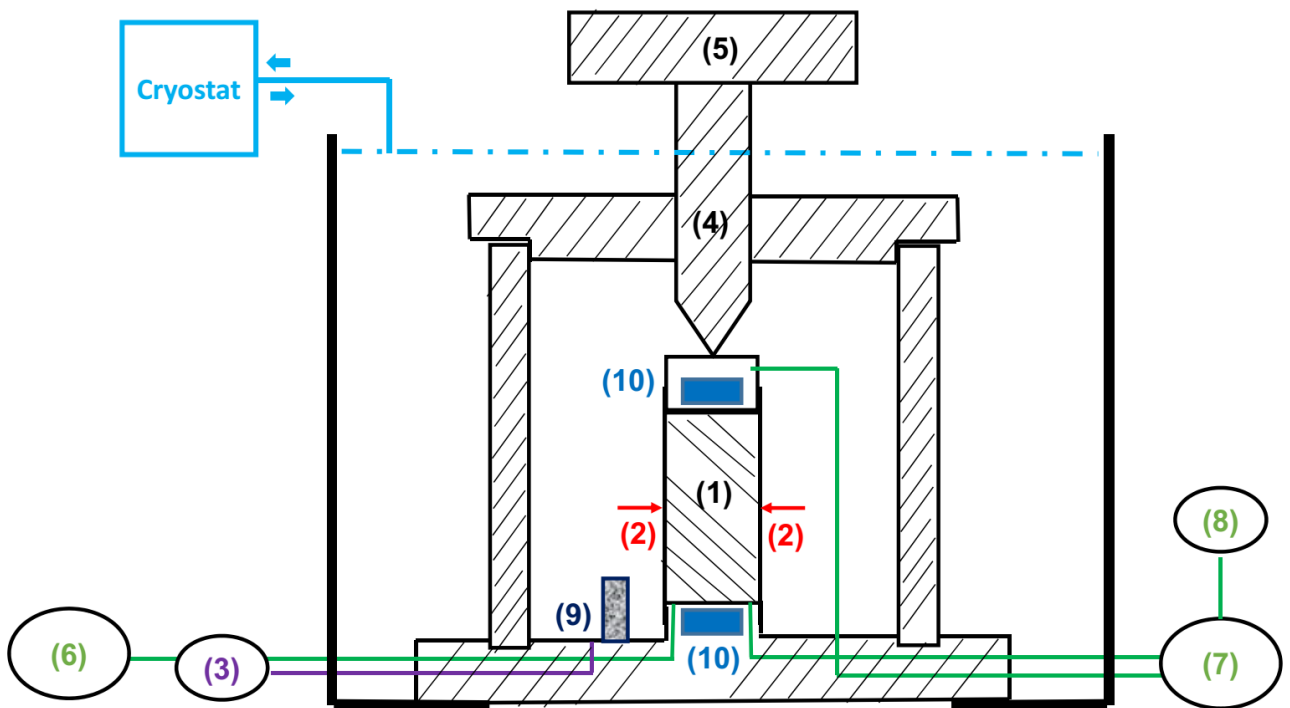
727

728   **Figure 2. Schematic diagram of the experimental setup**

729   (1): sample; (2): displacement sensor; (3): volume/pressure controller to control confining
730   pressure; (4): piston; (5): force transducer; (6): pressure transducer connected to gas flowmeter
731   for methane gas injection; (7): top and bottom pore pressure transducers connected by a T valve;
732   (8): volume/pressure controller to control pore pressure (water pressure); (9): thermocouple;
733   and (10): two ultrasonic sensors connected to a wave generator for measurement of V_P.
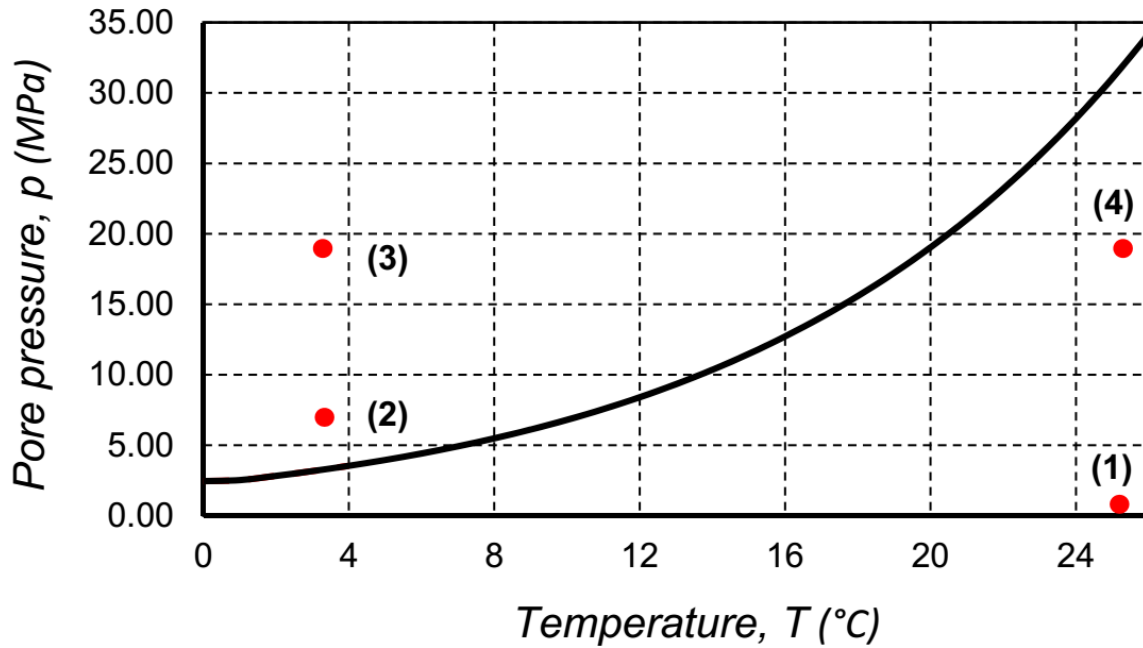
Figure 3. *p-T* conditions during gas hydrate formation

(1): Initial state of the sample (Step 1 and Step 2);

(2): *p-T* during GH formation in gas-saturated media (Step 3) and after water saturation (Step 4);

(3):

- Procedure A: *p-T* at the end of water saturation when confining pressure and pore pressure were increased to 22 MPa and 19 MPa, respectively;
- Procedure B: *p-T* during gas hydrate reformation;

(4): *p-T* at the end of gas hydrate dissociation for procedure B tests.

746
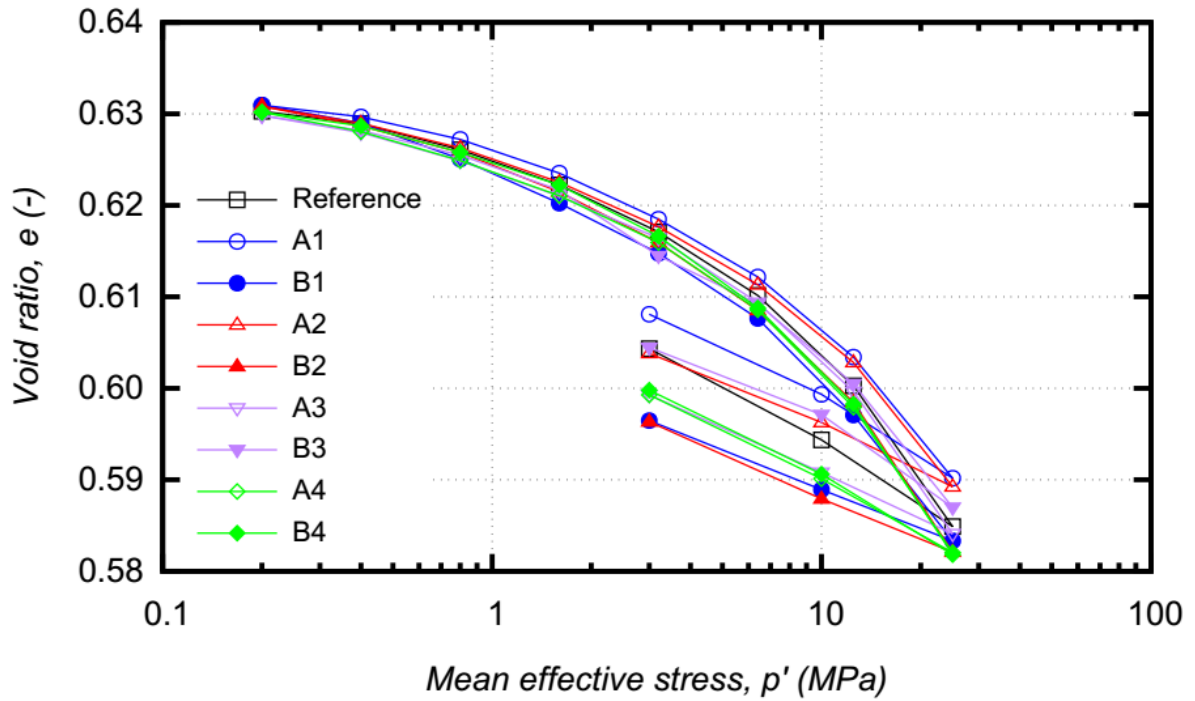
Figure 4. Void ratio versus effective stress for all tests

748
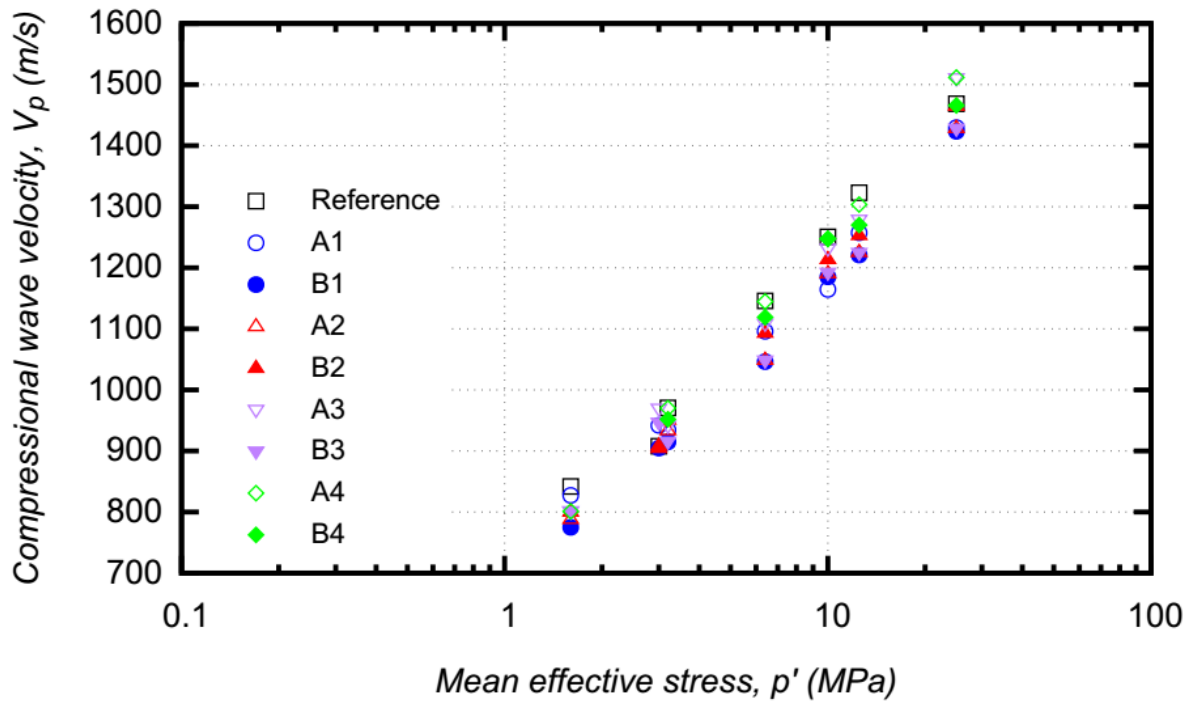
Figure 5. Compressional wave velocity versus effective stress for all tests

Induction time

750
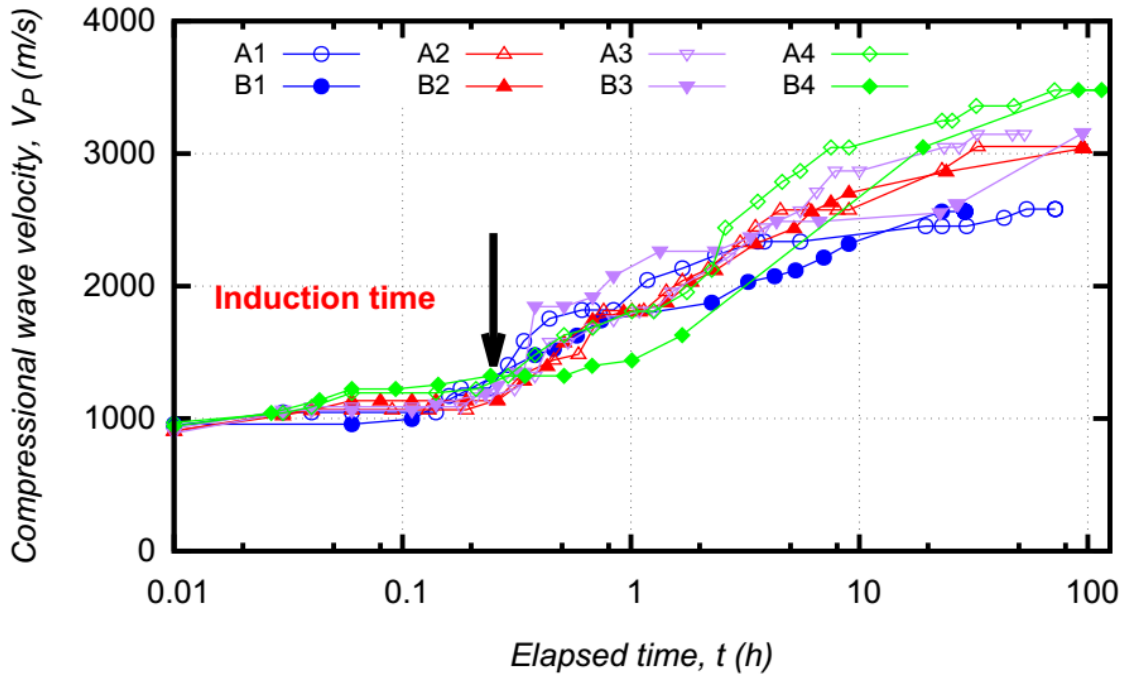
Figure 6. Compressional wave velocity versus elapsed time during methane hydrate
formation in gas-saturated media
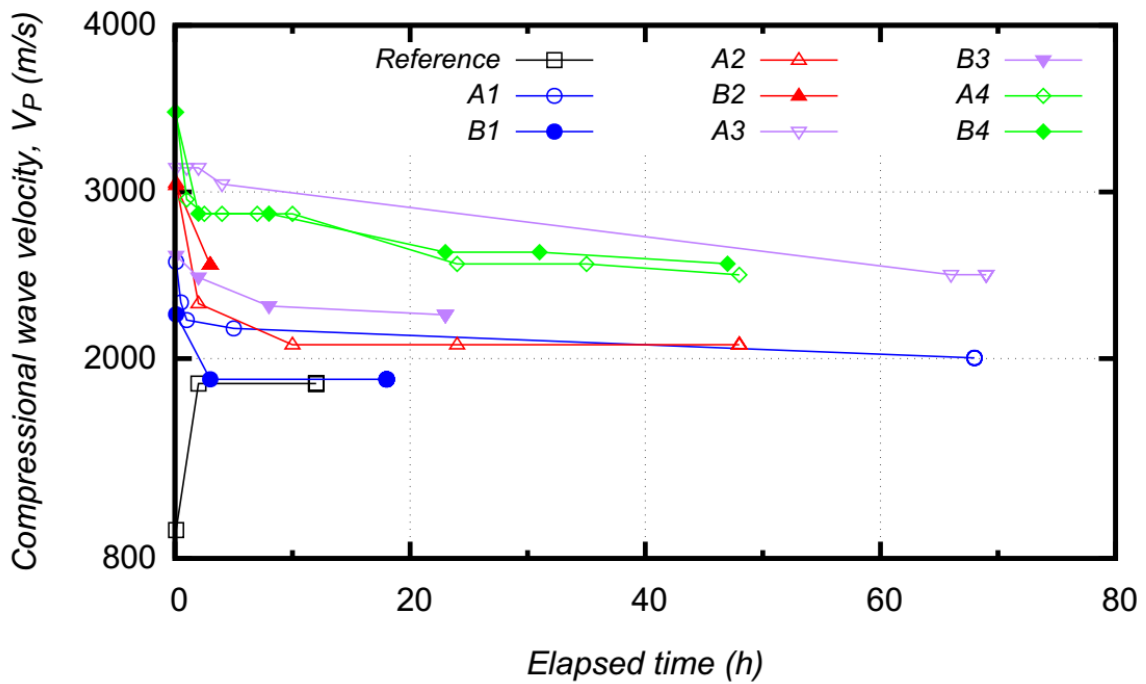
753

754   Figure 7. Compressional wave velocity versus elapsed time during water saturation

755

756
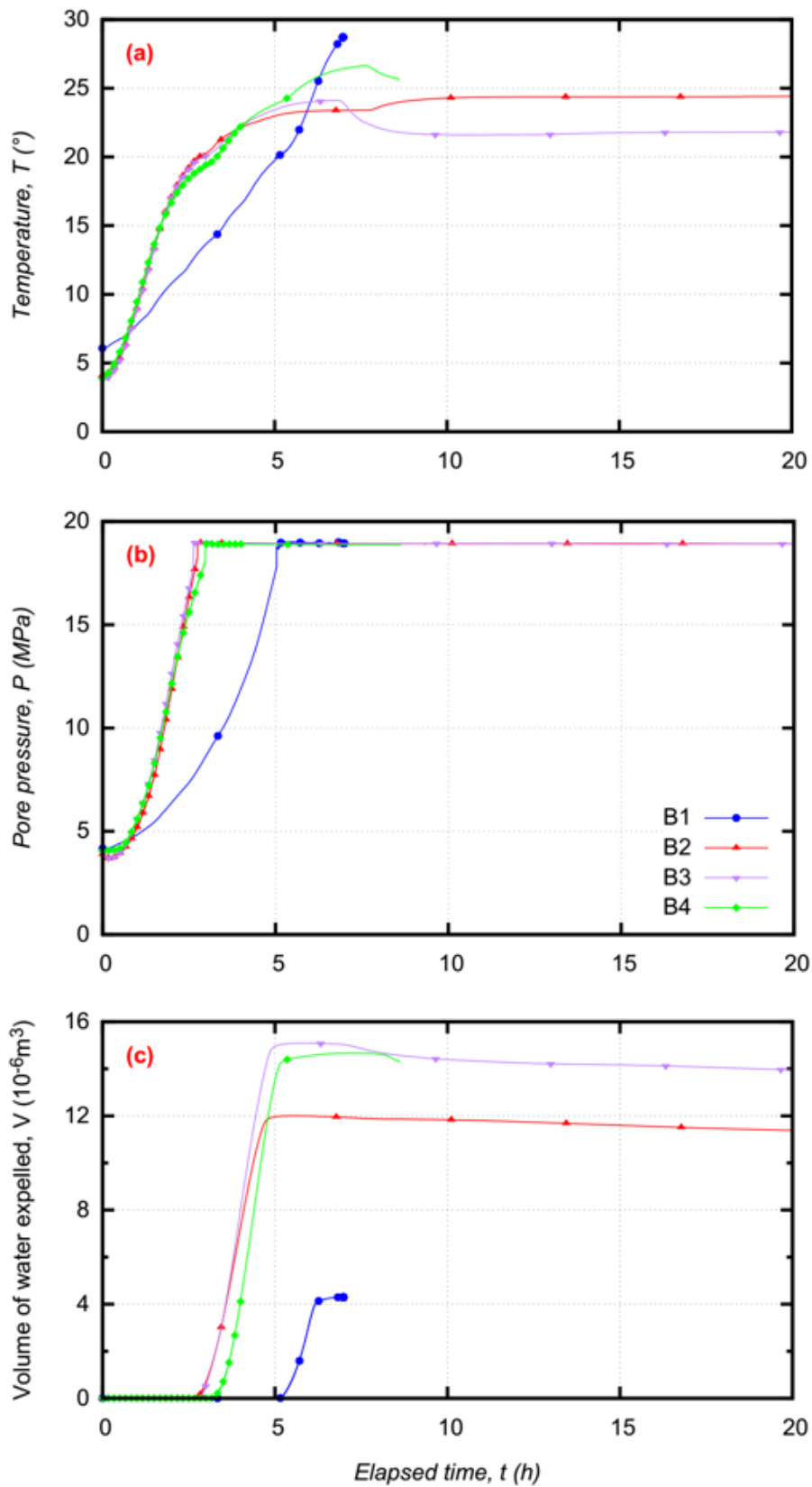
Figure 8. Pore pressure, temperature and volume of water expelled versus elapsed time during heating path

757
758

759

760
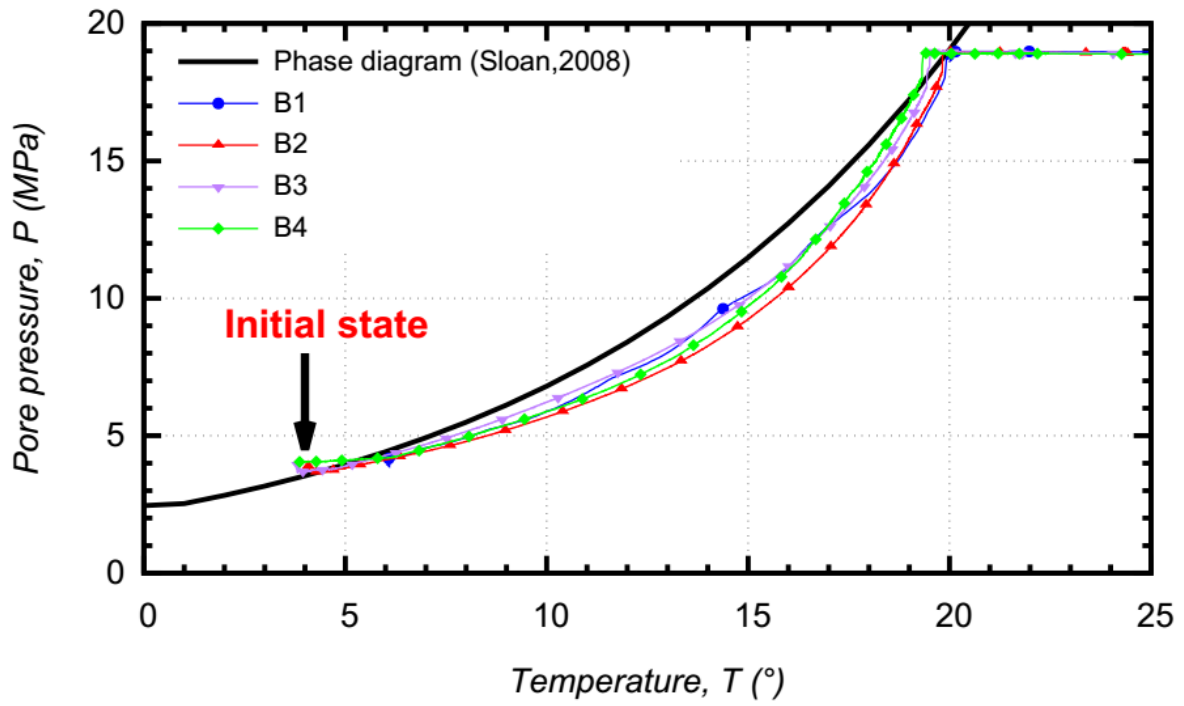
761

762   **Figure 9. Pore pressure versus cell temperature during dissociation**

763

764
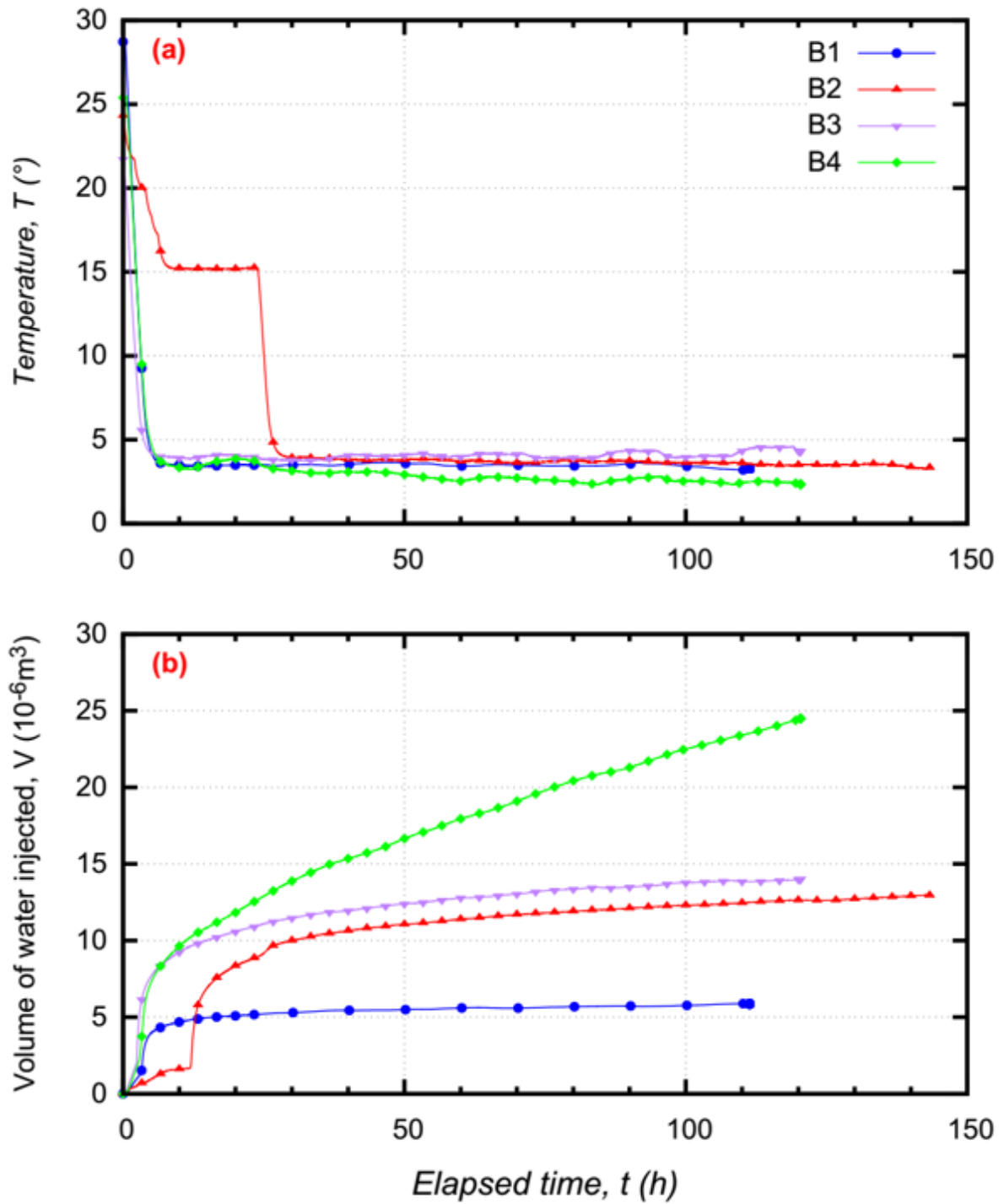
Figure 10. Temperature and volume of injected water versus elapsed time during hydrate reformation

769
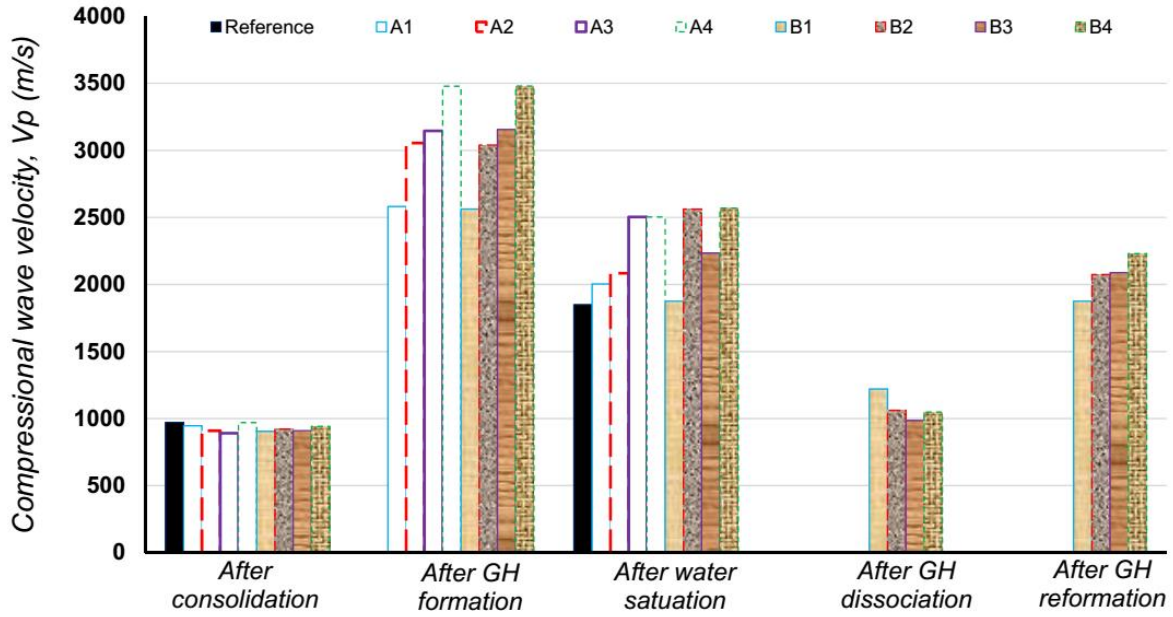
Figure 11. Compressional wave velocity during the whole methane hydrate formation of all tests

772

773
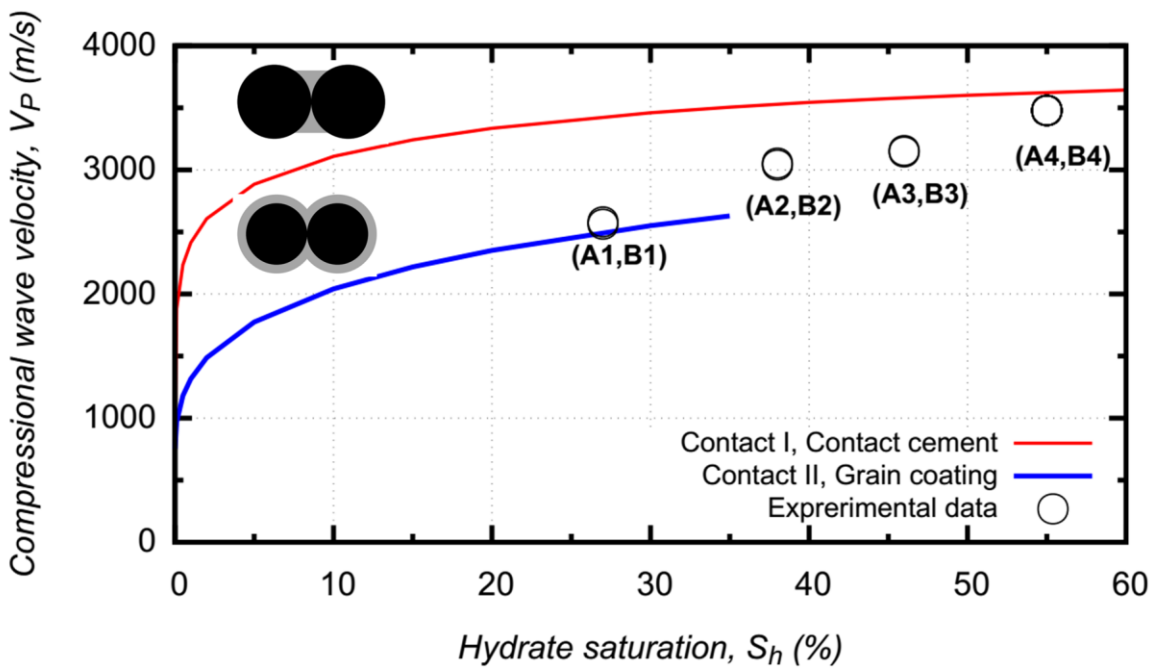
Figure 12. Comparison between experiments and Helgerud's model of compressional wave velocity dependence on methane hydrate saturation in gas-saturated media
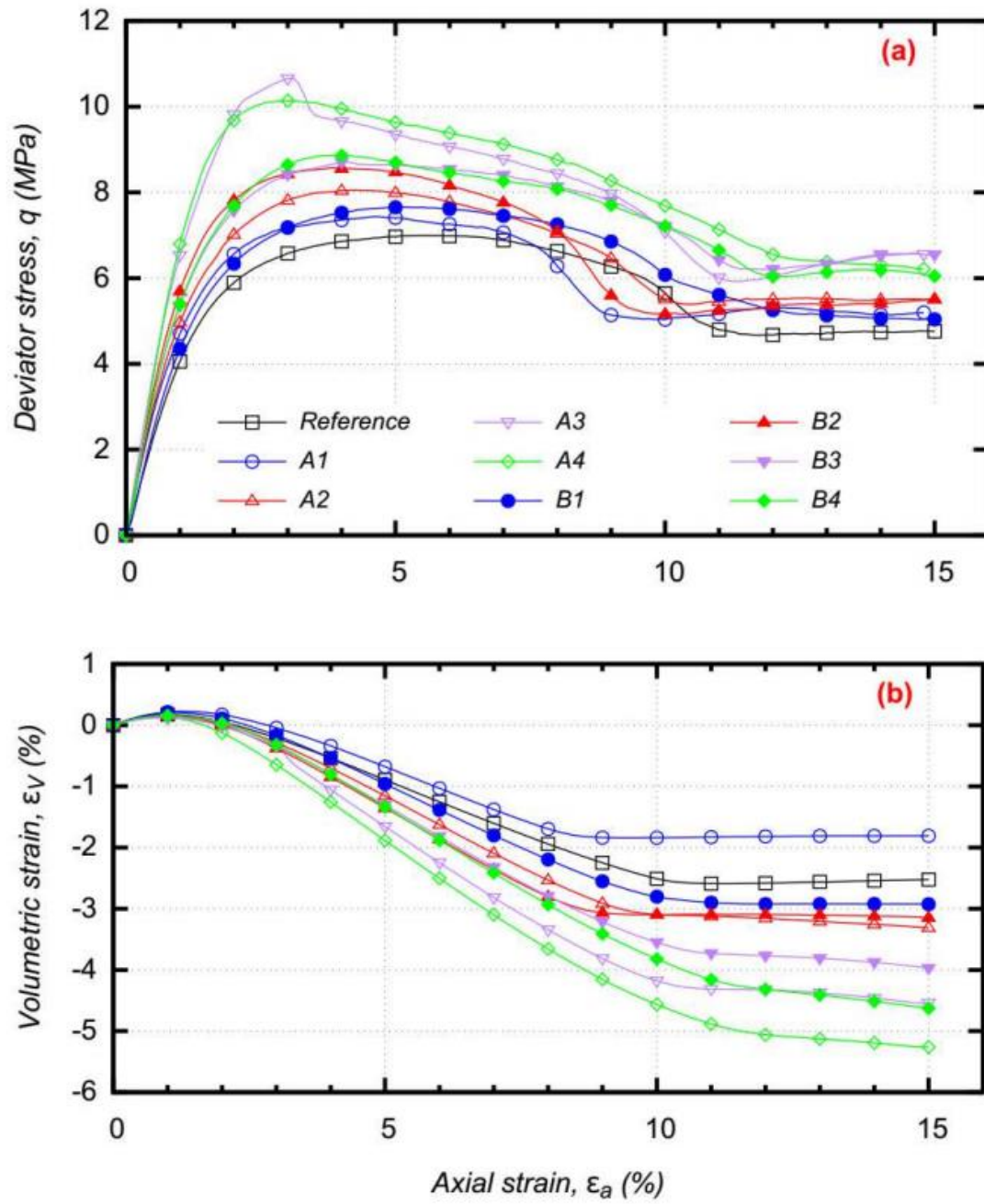
776
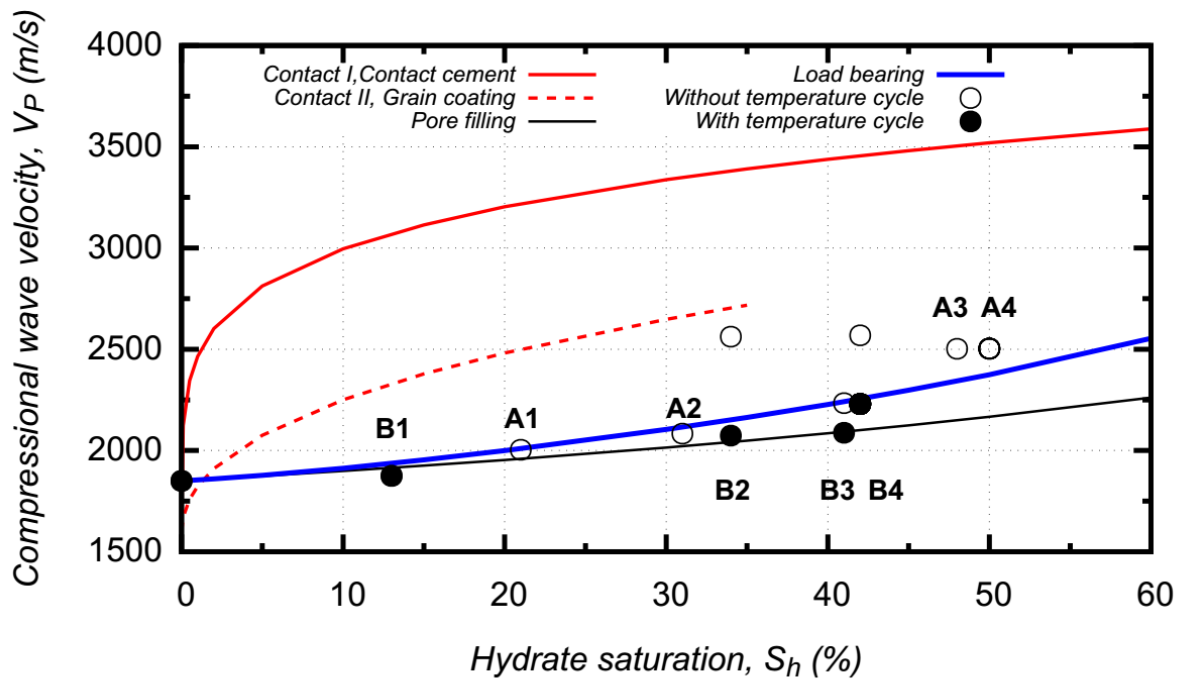
Figure 13. Comparison between experiments and Helgerud's model of compressional wave velocity dependence on methane hydrate saturation in water-saturated media
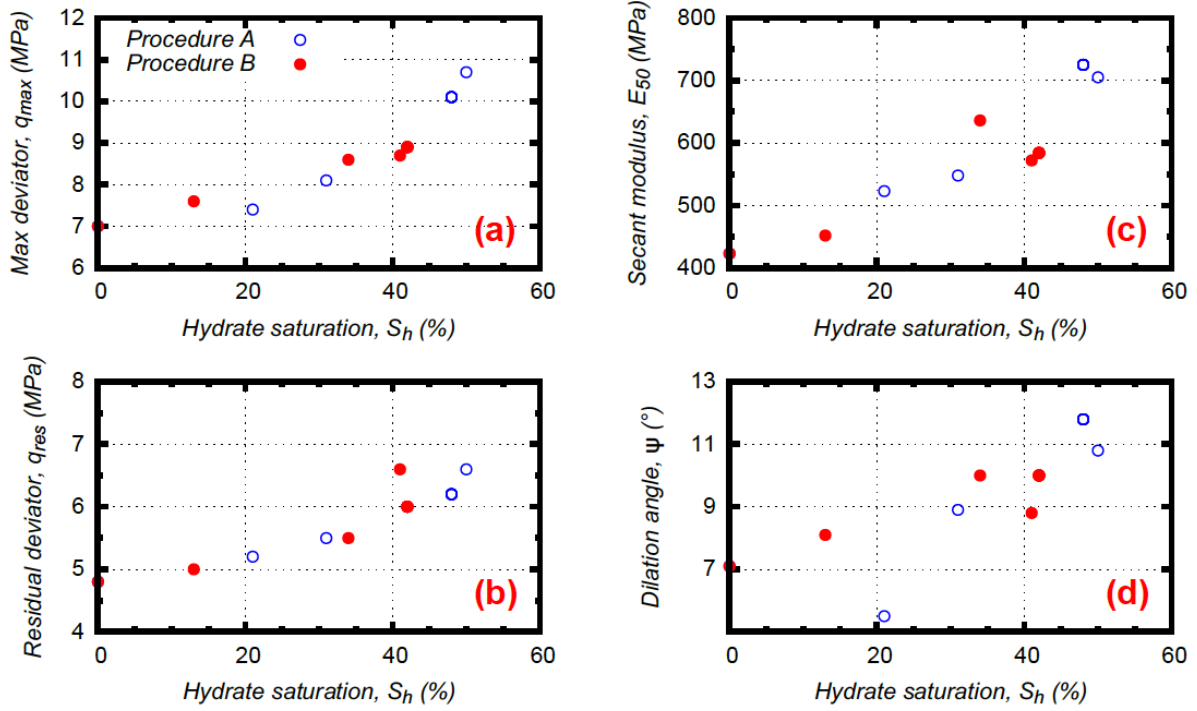
782

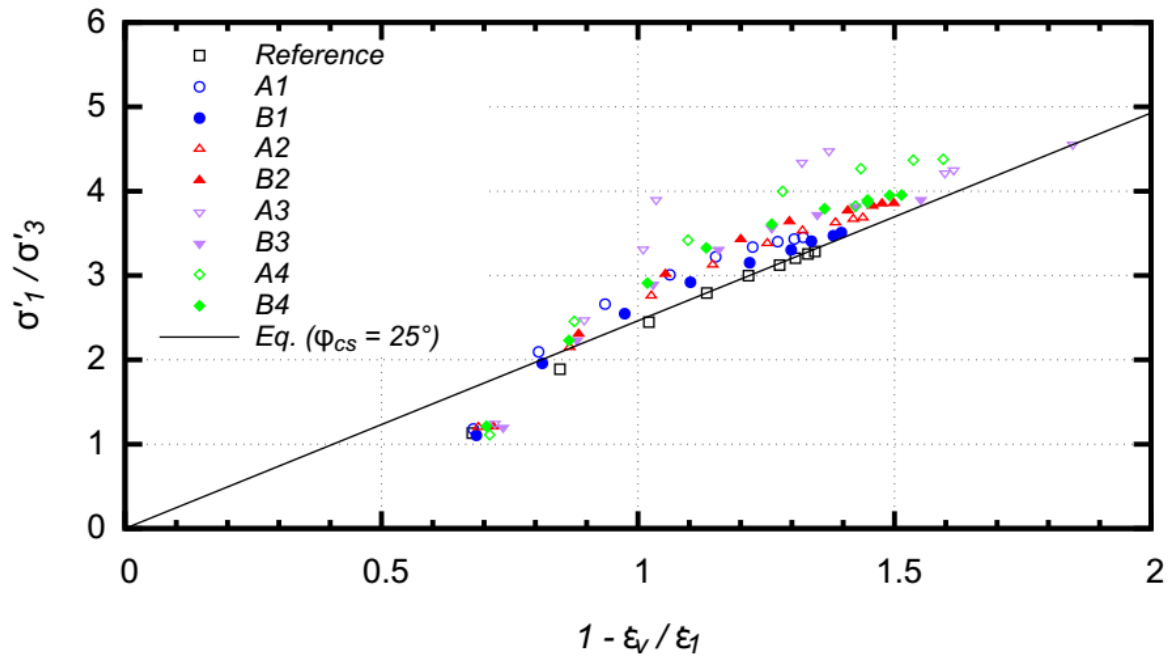783 **Figure 14. Deviator and volumetric strain versus axial strain**

784

785

Figure 15. Dependence of mechanical properties of sand on methane hydrate saturation for all tests

788

Figure 16. σ'_1/σ'_3 versus $1 - \dot{\varepsilon}_v/\dot{\varepsilon}_1$

790